Simulating the role of biogeochemical hotspots in driving nitrogen export from dryland watersheds

[1]Jianning Ren, [1]Erin J. Hanan, [2]Aral Greene, [3]Christina Tague, [4]Alexander H. Krichels, [1]William D. Burke, [5]Joshua P. Schimel, [2]Peter M. Homyak

[1]Department of Natural Resources and Environmental Science, University of Nevada, Reno, 89501, Reno, USA

[2]Department of Environmental Sciences, University of California, Riverside, 92521, Riverside, USA

[3]Bren School of Environmental Science & Management, University of California, Santa Barbara, 93106, Santa Barbara, USA

[4]USDA Forest Service Rocky Mountain Research Station, 87102, Albuquerque, USA

[5]Department of Ecology, Evolution and Marine Biology, University of California, Santa Barbara, 93106, Santa Barbara, USA

Correspondence:

Jianning Ren (nren@unr.edu, renjianning@gmail.com)

Erin Hanan (ehanan@unr.edu)

Key Points:

- We developed a model framework to represent biogeochemical hotspots in dryland ecosystems.
- Nitrogen export is sensitive to parameters controlling hotspot abundance, subsurface hydrologic connectivity, and soil moisture dynamics.
- The abundance and physical characteristics of hotspots can affect the timing of hot moments.

Abstract

Climate change and nitrogen (N) pollution are altering biogeochemical and ecohydrological processes in dryland watersheds, increasing N export, and threatening water quality. While simulation models are useful for projecting how N export will change in the future, most models ignore biogeochemical "hotspots" that develop in drylands as moist microsites become hydrologically disconnected from plant roots when soils dry out. These hotspots enable N to accumulate over dry periods and rapidly flush to streams when soils wet up. To better project future N export, we developed a framework for representing hotspots using the ecohydrological model RHESSys. We then conducted a series of virtual experiments to understand how uncertainties in model structure and parameters influence N export. Modeled export was sensitive to the abundance of hotspots in a watershed, increasing linearly and then reaching an asymptote with increasing hotspot abundance. Peak streamflow N was also sensitive to a soil moisture threshold at which subsurface flow from hotspots reestablished, allowing N to be transferred to streams; it increased and then decreased with an increasing threshold value. Finally, N export was generally higher when water diffused out of hotspots slowly. In a case study, we found that when hotspots were modeled explicitly, peak streamflow nitrate export increased by 29%, enabling us to better capture the timing and magnitude of N losses observed in the field. N export further increased in response to interannual variability in precipitation, particularly when multiple dry years were followed by a wet year. This modeling framework can improve projections of N export in watersheds where hotspots play an increasingly important role in water quality.

1 Introduction

Climate change and atmospheric nitrogen (N) deposition are accelerating biogeochemical cycling in dryland ecosystems and increasing N loading in streams, which can pose a major threat to water quality (Borer & Stevens, 2022; Fenn et al., 2003). However, the extent to which deposited N is exported to streams remains difficult to predict, in part because models are limited in their ability to capture hotspots—defined as wetter microsites in the soil that have disproportionately high rates of biogeochemical cycling—which can strongly influence N fluxes in dryland soils (Vargas et al., 2013). For example, hotspots enable N to accumulate over dry periods and rapidly flush to streams when soils wet up (McClain et al., 2003; Parker & Schimel, 2011). This can occur even when plants are N-limited because precipitation pulses can mobilize accumulated N more quickly than plants are able to take it up (Homyak et al., 2014). As the global distribution of drylands expands with climate warming (Seager et al., 2018), and as urbanization increases rates of N deposition (Borer & Stevens, 2022), it is critical to better account for the mechanisms driving N export in models (Gustine et al., 2022; Schimel, 2018).

Hotspots can range in size from microsites within soil aggregates (Ebrahimi & Or, 2018) to islands of fertility within landscape patches (Osborne et al., 2020). While landscape models may effectively represent the later by parameterizing plant physiological processes that promote resource heterogeneity—for example, transpiration-driven nutrient accumulation beneath woody plant canopies in savannas; (Ridolfi et al., 2008)—representing the role of microscale biogeochemical hotspots is much more challenging at watershed scales. For one, soil moisture and subsurface transport processes are often oversimplified and not fully integrated into landscape-scale N-cycling models (Ouyang et al., 2017; Poblador et al., 2017; Schmidt et al., 2007; Zhang et al., 2018). When models do incorporate coupled hydrological-biogeochemical

68 processes, they often reduce spatial heterogeneity by averaging soil hydraulic parameters across
69 a basin (Crow et al., 2012; Lin et al., 2015; Tague, 2009; Zhu et al., 2012, 2015). As a result,
70 these models do not capture the role of soil microsites that remain wetter than bulk soils for at
71 least some time into the dry season. While more detailed representation of soil heterogeneity is
72 needed, at least three key uncertainties remain in scaling microsite processes across an entire
73 watershed: (1) how hotspots are distributed across watersheds (McClain et al., 2003) (2) the
74 amount of precipitation required to reestablish for hydrological connection between hotspots and
75 bulk soils and to generate subsurface flow (Zhu et al., 2018), and (3) how the physical
76 parameters governing fine-scale water diffusion from hotspots are distributed across a watershed
77 (Clark et al., 2017).

78 A common modeling approach to represent the effects of fine-scale spatial heterogeneity
79 on large-scale hydrologic fluxes is to incorporate distributions of sub-grid state variables that
80 influence large-scale fluxes (i.e., statistical-dynamical flux parameterizations occurring within a
81 grid cell; the smallest spatially explicit model unit; Clark et al., 2017; Wood et al., 1992). For
82 example, Burke et al. (2021) developed an approach using the ecohydrological model RHESSys,
83 which uses a distribution of aspatial, sub-grid vegetation patches that interact to influence grid-
84 scale ecohydrological processes. This approach can better capture spatial heterogeneity without
85 requiring detailed spatial information at sub-grid scales or increasing computational costs. To
86 better predict how climate change modifies N retention and export, we developed a framework
87 for modeling belowground hotspots and their interactions with soil moisture and subsurface flow
88 by expanding the Burke et al. (2021) aspatial approach.

89

Our new modeling framework enables N to accumulate in microscale hotspots—represented aspatially within 10-m resolution grid cells—which contain sufficient moisture for decomposition to occur but are hydrologically disconnected from roots when the soils dry out. These micro-scale hotspot patches slowly lose water through diffusion and evaporation over the course of the dry season and can become hydrologically reconnected to the surrounding vegetated patches when soils wet up. Using this framework, we conducted a set of virtual experiments in a dryland, chaparral watershed in Southern California to characterize model sensitivity to three key sources of uncertainty: (1) the area percentage of hotspots within the watershed, (2) the length of time it takes for water to diffuse from hotspots during periods of drought, and (3) the moisture conditions under which hydrological connectivity between hotspot and non-hotspot locations reestablishes. Finally, we used field observations of N export to optimize the parameters controlling N dynamics and then with an optimized model, we investigated how precipitation patterns can influence hotspot effects on N export. This case study demonstrates how our modeling framework can be used to improve our theoretical understanding of the role biogeochemical hotspots play in N cycling and retention in drylands.

2 Methods

2.1 Study area

Model simulations were conducted in the Bell 4 basin (0.14 km^2), which is part of the San Dimas experimental forest located northeast of Los Angeles, California (34°12′N, 117°47′E; Figure 1). Elevations in Bell 4 range from 700 to 1024 meters. The topography is characterized by steep slopes with steep channel gradients. Soils are shallow, coarse-textured sandy loams, which are weathered from granite (Chaney et al., 2016; Dunn et al., 1988) and classified as Typic Xerorthents (Soil Survey Staff, 2022) The region has hot, dry summers (June to September

around 17 mm precipitation) and cool, moist winters (698 mm precipitation); mean annual precipitation is around 715 mm and daily temperatures range from -8 °C to 40 °C. Vegetation cover is mainly mixed chaparral with chamise (*Adenostoma fasciculatum*), ceanothus (*Ceanothus spp*.), and black sage (*Salvia mellifera*) on south-facing slopes; ceanothus and California laurel (*Umbellularia californica)* on north-facing slopes; and some live oak (*Quercus agrifolia*) along riparian areas (Wohlgemuth, 2006).

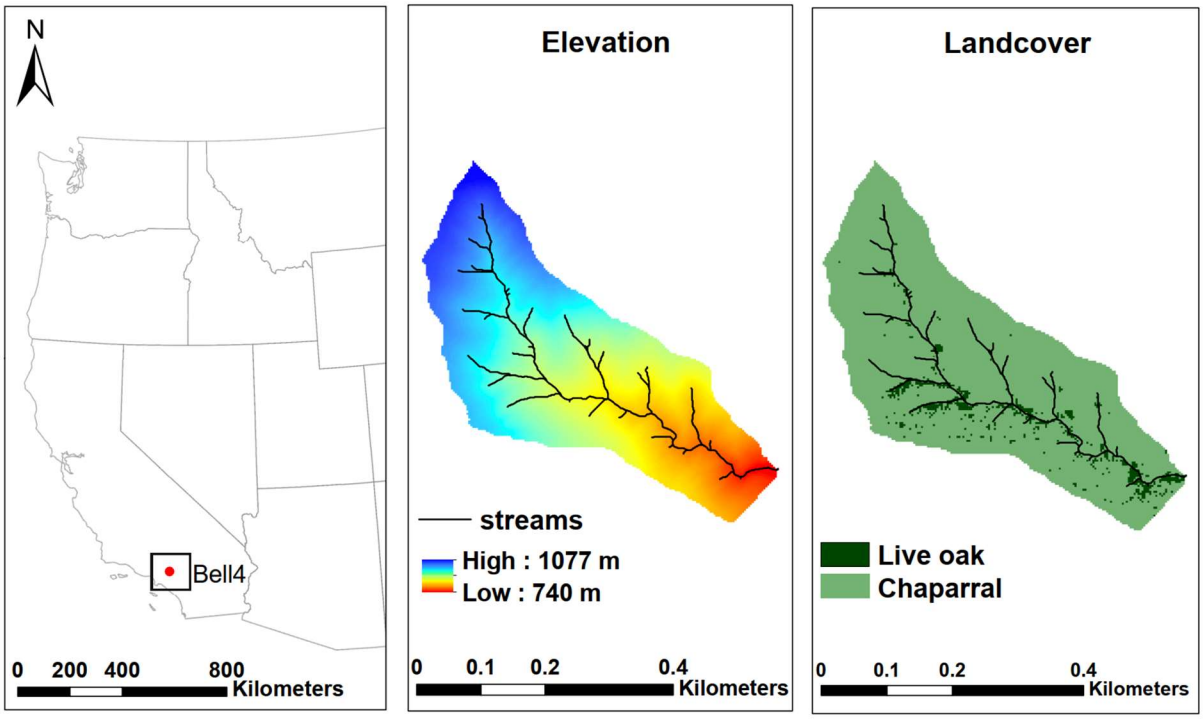

Figure 1. Bell 4 watershed in the San Dims experimental forest located in Southern California, U.S. (34°12′N, 117°47′E). The watershed is 0.14 km^2.

2.2 RHESSys model

The regional hydro-ecologic simulation system (RHESSys) is a spatially distributed, process-based model that simulates interacting ecohydrological and biogeochemical processes at multiple scales (Chen et al., 2020; Hanan et al., 2017; Tague, 2009; Tague & Band, 2004). The smallest spatial unit is the "patch," which has a 10-meter resolution in the current study. At the

patch scale, vertical hydrologic fluxes include canopy interception, transpiration, evaporation, infiltration, capillary rise, and drainage from the rooting zone to the saturated zone. Carbon (C) cycling processes are tightly coupled with hydrology and soil moisture and include photosynthesis, allocation of net photosynthate, plant and soil respiration, and litter and soil decomposition. Nitrogen cycling includes atmospheric N deposition, mineralization, nitrification, immobilization, denitrification, plant uptake, and export to streams (Hanan et al., 2017; Lin et al., 2015). RHESSys has been parameterized and validated in several watersheds across the western USA, including in several chaparral watersheds (Burke et al., 2021; Chen et al., 2020; Hanan et al., 2017, 2021; Lin et al., 2015; Meentemeyer & Moody, 2002; Ren et al., 2021, 2022; Tague, 2009).

There are four layers for vertical soil moisture processes, including a surface detention store, a root zone store, an unsaturated store below the root zone, and a saturated store. The vertical hydrologic processes also include canopy layers, snowpack, and litter moisture stores. Rain throughfall from multiple canopy layers and a litter layer provide potential infiltration. If the precipitation falls as snow, snow throughfall updates a snowpack store. Then the surface detention storage receives water from canopy throughfall and snowmelt at a daily time step. Following precipitation and throughfall, water infiltrates into the soil following the Phillip (1957) infiltration equation. At a daily timestep, ponded water that has not infiltrated is added to detention storage and any water that is above detention storage capacity generates overland flow.

Infiltration updates one of three possible stores: a saturated store when the water table reaches the surface, a rooting zone store, or an unsaturated store for unvegetated patches. A portion of infiltrated water can bypass the rooting zone and unsaturated store through macropores. This bypass flow (carrying N) is added to a deeper groundwater store at the

150 subbasin scale. Water drains vertically from the unsaturated store or root zone store based on
151 hydraulic conductivity. Capillary rise moves water from the saturated zone to the root zone or
152 unsaturated store based on Eagleson (1978). Lateral fluxes can occur through both shallow
153 subsurface flow between patches and through bypass flow that contributes to a deeper hillslope-
154 scale groundwater flow model. Shallow subsurface saturated flow between patches follows
155 topography and changes with saturation deficit and transmissivity.

156 RHESSys simulates subsurface lateral redistribution of water and N between patches
157 based on topographic gradients and soil hydraulic parameters (Tague, 2009). Nitrification rates
158 in RHESSys are calculated based on the CENTURY$_{NGAS}$ model, where the nitrification rate is a
159 function of soil pH (f_{pH}; Hanan et al 2017), moisture (f_{H_2O}), soil temperature (f_T), and available
160 soil ammonium (f_{NH_4}; Parton, 1996):

161 $$N_{nitrif} = soil.NH4 \times f_{pH} \times f_{H_2O} \times f_T \times f_{NH_4} \quad \text{Eq (1)}$$

162 The pH scalar (f_{pH}) is calculated as:

163 $$f_{pH} = \frac{0.56 + arctan\,(\pi \times 0.45 \times (-5 + pH))}{\pi} \quad \text{Eq (2)}$$

164 The soil moisture scalar (f_{H_2O}) is calculated as:

165 $$f_{H_2O} = (\frac{\theta - b}{a - b})^{d(\frac{b-a}{a-c})} (\frac{\theta - c}{a - c})^{d} \quad \text{Eq (3)}$$

166 Where *a*, *b*, *c*, and *d* are parameters related to soil texture based on Parton et al. (1996) and θ is
167 volumetric soil moisture.

168 The temperature scalar (f_T) is calculated as:

169 $$f_T = 0.06 + 0.13exp^{0.07T_{soil}} \quad \text{Eq (4)}$$

Where T_{soil} is the surface soil temperature in degrees C.

The ammonium concentration available for nitrification is calculated as:

$$f_{NH_4} = 1.0 - exp^{[-0.0105 * NH_{4conc}]} \quad \text{Eq (5)}$$

Where NH_{4con} is the soil ammonium concentration in the fast-cycling soil layer.

N export includes denitrification and subsurface lateral flow of ammonium, nitrate, and dissolved organic N (DON). Denitrification is calculated based on a maximum denitrification rate (R_{NO_3}), and is modified by soil moisture (f_{H_2O}), and soil respiration (f_{hrCO_2}):

$$N_{denitrif} = R_{NO_3} \times f_{H_2O} \times f_{hrCO_2} \quad \text{Eq (6)}$$

The maximum denitrification rate is calculated as:

$$R_{NO3} = 0.0011 + \frac{a\,tan\,(\pi \times 0.002 \times \left(\frac{NO_{3\_soil}}{N_{soil}+C_{soil}} - 180\right))}{\pi} \quad \text{Eq (7)}$$

Where NO_{3_soil} is the available nitrate (kg N/m^2) in soil and N_{soil} and C_{soil} are soil N (kg N/m^2) and C (kg C/m^2) amounts, respectively.

The soil moisture limitation is calculated as:

$$f_{H_2O} = \frac{a}{b^{\left(\frac{c}{b^{d \times \theta}}\right)}} \quad \text{Eq (7)}$$

θ, a, b, c, and d are defined in eq. 3 above.

The effect of soil respiration is calculated as:

$$f_{hrCO_2} = \frac{0.0024}{1 + \frac{200}{e^{(3.5 \times hr)}}} - 0.00001 \quad \text{Eq (8)}$$

Where hr is total daily respiration (g C/m^2/day).

188 Nitrate enters the soil from infiltration or from the surface detention store. Nitrate in the
189 soil is transported by subsurface flow in the saturated zone, while in the unsaturated soil, there is
190 no lateral nitrate transport (Chen et al., 2020; Tague & Band, 2004). Vertical distribution of
191 nitrate in the unsaturated zone soil profile is assumed to follow an exponential decay function,
192 where the surface layer has more nitrate and deeper soil has less. the available nitrate at soil
193 depth z is calculated as

194 $$NO_{3\_soil}(z) = NO_{3\_surface} \times exp^{-N_{decay} \times z} \quad \text{Eq (10)}$$

195 Where $NO_{3\_surface}$ is nitrate at soil surface and N_{decay} is a soil specific parameter that defines the
196 rate of nitrate decay. When water is moving between the unsaturated zone and the saturated
197 zone, through downward leaching or upward capillary rise, nitrate moves with water based on its
198 concentration.

199 Nitrate export follows the flushing hypothesis (Chen et al., 2020). As the water table rises, more
200 N becomes available for flushing. The total soil nitrate export (NO_{3_out}) is calculated as the
201 integration of soil nitrate below the water table:

202 $$NO_{3\_out} = \int_{z_{max}}^{z_s} \frac{q_z}{S_z} NO_{3\_soil} NO_{3\_mobile} \quad \text{Eq (11)}$$

203 Where z_{max} is the maximum water table depth, z_s is current water table depth, q_z is the net lateral
204 transport of water from the patch at depth Z; S_z is the soil water content (in meters) and NO_{3_mobile}
205 is a parameter that defines the portion of nitrate that is mobile (related to soil type). Mobile
206 surface N can also be transported to deep ground water through preferential flow paths.

207 Recent improvements to RHESSys enable users to account for fine-scale (within patch)
208 heterogeneity (e.g., different types of vegetation cover and associated soil layers that may share

water within a single patch; Burke et al. 2021). These are referred to as "aspatial patches." When running RHESSys using the aspatial patch framework, “patch families” become the smallest spatially explicit model unit, and aspatial patches (nested within a patch family) are the smallest aspatial model unit. Note that an aspatial patch within a patch family is used to represent a distribution of a given vegetation type (e.g., trees or shrubs) based on observed (or hypothetical) distributions. It can but does not necessarily represent a single stand or clump of vegetation cover; vegetation from a single aspatial patch within a patch family does not have a defined distribution in RHESSys, so the assumption is that biophysical interactions, such as the extent to which a given cover type shares water, are more important than their physical location within the finest grid cell. Because there are no physical locations of aspatial patches within a patch family, within patch heterogeneity can be modeled without explicitly parameterizing and modeling fine scale spatial units that would be both computationally prohibitive and nearly impossible to parameterize with measured data.

Local water routing between aspatial patches inside a patch family is based on root access to water (Figure 2). Local routing moves water between aspatial patches based on user defined rules. Most commonly, water is distributed among aspatial patches as a function of relative differences between their rooting and unsaturated zone water contents and mediated by gaining and losing coefficients defined for each cover type. In this framework, an aspatial patch will gain water if its water content is below the patch family mean and vice versa, with the rate of water transfer controlled by sharing coefficients. Sharing coefficients to capture the integrated effects of uncertain, fine-scale variation in root distributions, and how root distributions and forest structure interact with fine-scale soil drainage characteristics. Nitrate and dissolved organic C are

exchanged along with water during local routing. A detailed description of aspatial patches can be found in Burke et al. (2021).

2.3 Model development

To enable RHESSys to account for biogeochemical hotspots, we expanded the aspatial patch framework to incorporate "hotspot" aspatial patches within each patch family. These aspatial patches represent a distribution of unvegetated microsites where biogeochemical cycling can be hydrologically disconnected, as soils dry out, from aspatial patches that contain plant roots (Figure 2). To model hotspot aspatial patches (hereafter called hotspots), we implemented three key model developments: (1) model algorithms that enable hotspots to access soil and litter C and N from neighboring non-hotspot patches for decomposition and biogeochemical cycling, and (2) algorithms and parameters that control the moisture conditions under which hotspots are hydrologically disconnected from other aspatial patches in the saturated zone, (3) parameters that control water diffusion in the unsaturated and/or root zone between hotspot and non-hotspot patches as soils dry out.

Research has shown that N-rich microsites can occur in unvegetated locations where there is less N uptake and less water demand from plants (Zhu et al., 2018). In the original RHESSys framework, unvegetated patches were used to represent large (e.g., 10 to 30-m) areas with no vegetation. Without vegetation inputs, these patches did not develop C and N stores to support microbial biogeochemical cycling. To generate hotspots, we implemented a litter sharing scheme that moves litter from vegetated aspatial patches to hotspots at an annual timestep to coincide with litter fall (Figure 2). Because we assume that hotspot aspatial patches occur at fine scales across a given 10-m patch family, it is reasonable to assume that they have access to plant litter for decomposition and N cycling from other aspatial patches within the patch family. The

amount of litter shared (CN_{share}) is a function of the mean litter C and N content of the patch family (CN_{mean}), where the amount of C and N in a hotspot patch after litter sharing ($CN_{hotspot}$) cannot be above the patch family mean (Eq 12). To enable N cycling in hotspots, hotspots also have access to 1% of the protected soil organic C and N pools from the vegetated patch families. The litter C and N routing is described as

$$CN_{share} = \frac{(\sum_{i=1}^{n_{veg}} (CN_{veg\_i} - CN_{mean}) \times coef\_litter)}{n_{hotspot}} \quad \text{Eq (12)}$$

$$CN_{hotsp\_after} = min\ (CN_{hotspot\_before} + CN_{share}\ ,\ CN_{mean}) \quad \text{Eq (13)}$$

$$CN_{veg\_after\_i} = CN_{veg\_i} - \left(CN_{veg\_i} - CN_{mean}\right) \times coef\_litter \quad \text{Eq (14)}$$

Where, n_{veg} is the number of non-hotspot patches in a patch family, CN_{veg} is the amount of litter C and N in a non-hotspot patch, $n_{hotspot}$ is the number of hotspot patches in a patch family. *Coef_litter* is the sharing coefficient parameter that controls the amount of litter sharing. Hotspot patches can also be assigned a finer soil texture (e.g., loam), which can hold more water than non-hotspot patches. In the current model, non-hotspot patches were comprised of sandy loam (based on the POLARIS database; Chaney et al., 2016).

To control subsurface hydrologic flow from hotspots to vegetated patches, we set up a soil moisture threshold for non-hotspot patches (θ_{th}), above which, water flows into them from the saturated zone in hotspots. In other words, when non-hotspot patches dry down, they become hydrologically disconnected from hotspots and they become reconnected when soils wet up (Figure 2c & Eq 15).

$$\begin{cases} \theta_{veg} > \theta_{th}: \textit{subsurface flow move water and nitrate from hotspots to neighboring non} - \textit{hotspot pathes} \\ \theta_{veg} \leq \theta_{th}: \textit{no subsurface flow from hotspots to neighbor normal patches} \end{cases} \quad \textbf{Eq (15)}$$

This threshold is used to define a condition where "water films" can form as soils dry down, which enables microscale biogeochemical cycling while reducing nitrate leaching from hotspots over the course of the hot, dry summer (Parker & Schimel, 2011). When soils are rewetted at the onset of the rainy season, the water table rises, and hydrologic connectivity reestablishes between hotspot and non-hotspot patches. This can lead to rapid nitrification and nitrate export before plants become active and gain access to N that accumulated during dry periods of hydrologic disconnection (Parker & Schimel, 2011). While the thresholds at which hydrologic connectivity reestablishes are not currently well established, the threshold parameter can be calibrated to match field observations.

Although subsurface flow from hotspot patches remains somewhat disconnected during the dry season, water can still slowly diffuse from hotspots as soils dry out. To account for this, we developed water gain coefficients (sh_g) and water loss coefficients (sh_l) that constrain local routing to and from hotspots and the unsaturated and rooting zone in the surrounding non-hotspot patches (Figure 2a). During the dry season (June to November), the default sh_g was set to 0.05 and sh_l was set to 0.9 to simulate hotspots losing water. During the wet season (December to May), the default sh_g was 0.9 and sh_l was 0.05 to simulate hotspots gaining water. We rely on sharing coefficients here to capture "film" dynamics that depend on micro-scale characteristics that are not feasible to explicitly model but have been documented to influence hot-spot dynamics in field and lab-studies (Homyak et al., 2016; Parker & Schimel, 2011). To summarize, while soil moisture gradients control whether routing occurs in the saturated zone between hotspot and non-hotspot patches, the sharing coefficients control the rate of local water transfer in the unsaturated zone.

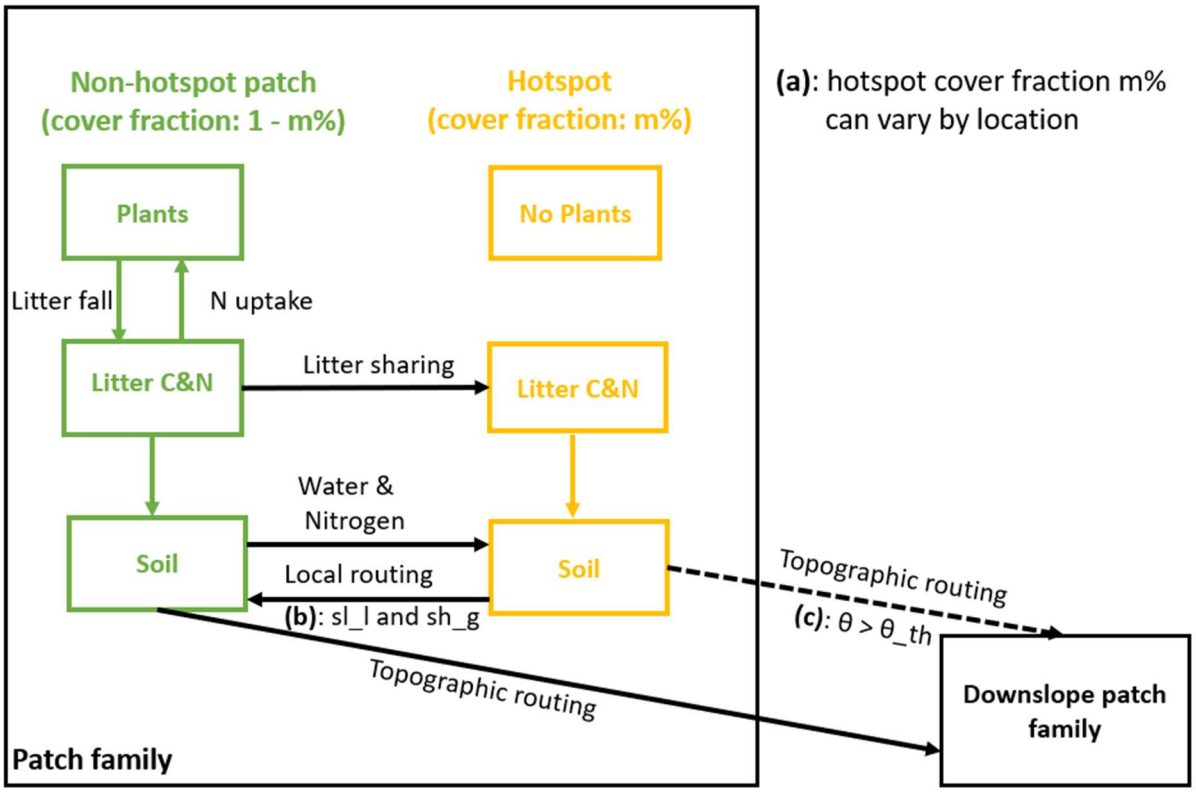

Figure 2. Conceptual overview of hotspots patches nested within each patch family. Each year, vegetated patches share litter C and N with hotspot patches from the portions of their stores that are greater than the patch family means. Note that the conceptual figure does not indicate that there is only one hotpot and one non-hotspot patch in a patch family, but rather represents their cover fraction. Key model uncertainties include: (a) hotspot cover fraction m%, which can vary by location, (b) local routing of water and N in the unsaturated zone between aspatial patches based on the mean water content of the patch family, which can be mediated by sharing coefficients sh_l and sh_g; and (c) topographic routing in the saturated zone from patches in one patch family to patches in downslope patch families, which can be controlled by a soil moisture threshold θ_{th}. The dashed lines signify that hotspots are hydrologically disconnected from non-hotspot patches during dry periods but reconnect during wet periods when soil moisture in non-hotspot patch is larger than θ_{th}. The extent of hydrological routing between hotspot and non-hotspot patches is controlled by θ_{th}, which can be calibrated to match field observations.

2.4 Data

To generate metrological inputs for RHESSys scenarios in Bell 4 using the new hotspot framework, we compared daily meteorological data from gridMET (Abatzoglou, 2013), including maximum and minimum temperatures, precipitation, relative humidity, radiation, and wind speed, from 1979 to 2020, to daily meteorological data at a station located near Bell 4 (San

Dimas Tanbark) from the U.S. Forest Service (USFS). Because gridMET matched closely with ground station data but does not require gap filling, gridMET was selected as a suitable meteorological forcing dataset for our analyses. To calibrate drainage parameters, we used streamflow data from the USFS for the years 1980 to 2002; data were missing for some months (Figure 3). We omitted 8 years of streamflow data (1984-1992) following a prescribed fire that occurred in 1984 (Meixner et al., 2006). We selected streamflow data from 1993 to 2002 for model calibration and 1980 to 1983 for validation (described in section 2.5 below).

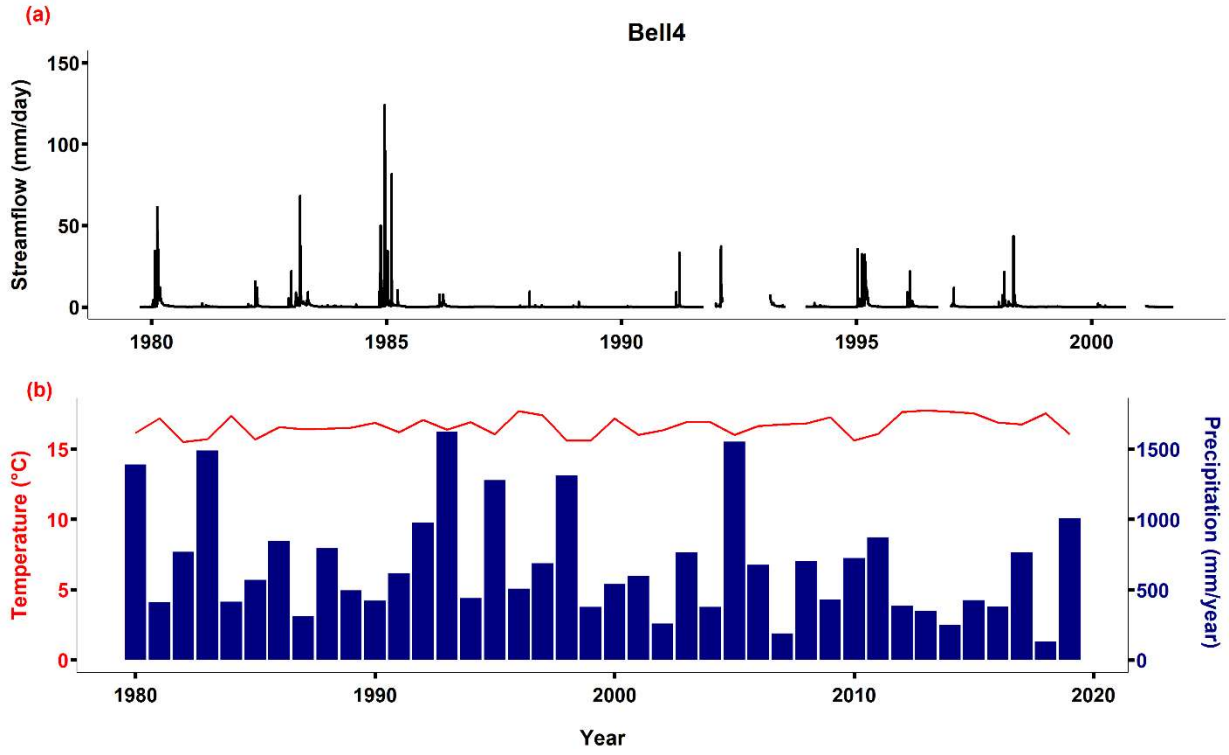

Figure 3. Streamflow and climate data for Bell 4. The temperature is yearly average, and streamflow is calculated as the volume divided by the catchment area (0.14 km^2).

We aggregated a 1-m resolution Digital Elevation Model (DEM) from LiDAR to 10 meters to represent topography across the watershed. To map landcover, we aggregated 1-m resolution land cover data from the National Agriculture Imagery Program (NAIP; collected on June 5, 2016) to 3-m and classified three land cover types: chaparral, live oak, and bare ground

(Maxwell et al., 2017). We then overlapped the 10-meter DEM with 3-meter vegetation cover data to classify aspatial patch distributions in each patch family using a k-means function (Hartigan & Wong, 1979) in R version 4.3.0 (R Core Team, 2022). This resulted in approximately 11 aspatial patches in each patch family and 375 different vegetation combinations across the watershed. We acquired soil texture data from POLARIS (Chaney et al., 2016).

To measure streamflow, two pressure transducers (Water level data loggers), compensated for barometric pressure (Barologgers; Solinst Canada Ltd, Georgetown, Ontario, Canada), were used to record stream stage at the Bell 4 weir. Water stage was measured at 5-minute intervals and converted to discharge using a rating curve developed for the v-notch weir. Stream samples were collected using an automatic sampler (Teledyne, ISCO model 6712C, Lincoln, Nebraska, US) set to collect 500-mL samples every 2 hours over a 48-hour period at the onset of flow. Samples were then filtered through pre-baked whatman GF/F filters and stored at -20 °C. Nitrate and ammonium concentrations were measured colorimetrically using an AQ2 SEAL discrete analyzer (methods EPA-129-A and EPA-126-A).

2.5 Model initialization, calibration, and evaluation

We initialized the soil C and N pools by spinning them up to steady state (i.e., running the model until the pools stabilized). For the vegetation C and N pools, we used a target-driven method that allows vegetation to grow until it reaches target leaf area index (LAI) values from remote sensing data (Hanan et al., 2018). This method enables C and N pools to spin up mechanistically while still capturing landscape heterogeneity resulting from local resource limitations and disturbance histories. To construct a map of target LAI values, we chose the

clearest available NAIP image during the growing season (i.e., April 24, 2010). We then calculated NDVI using equation 1.

$$NDVI = \frac{\rho_{NIR} - \rho_R}{\rho_{NIR} + \rho_R} \quad (1)$$

In this equation, ρ_{NIR} is the reflectance in the near-infrared, and ρ_R is reflectance in the red (Hanan et al., 2018). We then estimated LAI using a generalized NDVI-LAI model developed by (Baret et al. 1989; equation 2).

$$LAI = -\frac{1}{k} \times ln\left(\frac{NDVI_{max} - NDVI}{NDVI_{max} - NDV_{back}}\right) \quad (2)$$

Here, k is the extinction of solar radiation through a canopy. $NDVI_{max}$ is the maximum NDVI occurring in the region, and $NDVI_{back}$ is the background NDVI (i.e., from pixels without vegetation). We obtained k value from Smith et al. (1991) and White et al. (2000). The other parameters were obtained for each vegetation type (Table 1).

Table 1. Parameters used for calculating LAI from NDVI

Vegetation type	k	$NDVI_{max}$	$NDVI_{back}$
Live oak	0.500	0.379	-0.160
Chaparral	0.371	0.372	-0.160

We used observed streamflow for Bell 4 to calibrate six soil parameters: saturated hydraulic conductivity (K_{sat}), the decay of K_{sat} with depth (m), pore size index (b), air entry pressure (ϕ), bypass flow to deeper groundwater storage (gw_1), and deep groundwater drainage rates to stream (gw_2). We selected the best parameter set by comparing observed and modeled streamflow using monthly Nash-Sutcliffe efficiency (NSE; Nash & Sutcliffe, 1970) and percent

error in annual flow estimates. NSE is used to evaluate peak flows and can range from -∞ to 1, where 1 represents a perfect fit between modeled and observed data. Percent error is used to compare differences between the total quantity of modeled and observed streamflow; values closer to zero represent better fit.

2.6 Sensitivity analyses and simulation scenarios:

After model initialization and calibration, we used the new model framework to build in microscale hotspots. We assumed the hotspots were evenly distributed across the landscape and converted one bare ground patch inside of every patch family to an aspatial hotspot patch. Note that this does not mean that there was only one hotspot in a patch family, but one aspatial patch was used to represent the distribution (or percent cover) of microscale hotspots. If no bare ground patches existed in the patch family, we instead converted a chaparral patch to an aspatial hotspot patch. Because there were approximately 11 patches in each patch family, this setup resulted in approximately 9% of each patch family (and of the overall basin) consisting of microscale hotspots. We also assigned a loam soil texture to hotspot patches to represent the soil physical properties that may also increase moisture retention. The default parameters used to represent hotspot hydrological and biogeochemical dynamics are shown in Table 2.

Table 2. Default parameters for hotspots. Sh_l and sh_g control water diffusion in the unsaturated zone between hotspot and non-hotspot patches, the default values promote strong seasonality in hotspot soil moisture. The soil moisture threshold controls water flow in the saturated zone between hotspot and non-hotspot patches; the default value promotes the maximum peak streamflow N. We defined one aspatial patch as a hotspot inside of each family. This leads to 9.1% cover of hotspot patches evenly distributed across the landscape.

Parameters	Value
Sharing coefficient of losing water in unsaturated zone from hotspots (sh_l)	Dry season: 0.9 Wet season: 0.05
Sharing coefficient of gaining water in unsaturated zone of hotspots (sh_g)	Dry season: 0.05 Wet season: 0.9

Soil moisture threshold of non-hotspot above which water in saturated zone flows from hotspots to non-hotspot (θ_{th})	21%
Percentage cover of hotspots	9.1%
Sharing coefficient of litter from non-hotspot patches to hotspot patches (coef_litter)	1

391

392 To evaluate the uncertainties related to model structure and parameters, we conducted a set of
393 virtual experiments, or sensitivity analyses. For each sensitivity analysis, we ran RHESSys for 60
394 years by looping the available climate data from 1979-2020. Results are presented as simulation
395 years and capture the climate variability from the available record. First, we examined how the
396 percentage cover of hotspots can influence N export. We built hotspot patches from zero percent
397 to 13.7 percent at 2.3 percent increments (i.e., 0%, 2.2%, 4.5%, 6.8%, 9.1%, 11.4%, 13.7%).
398 When the hotspot percentage was equal to 9.1%, there were exactly one aspatial hotspot patch in
399 each patch family. When the hotspot percentage was larger than 9.1%, we needed to convert two
400 aspatial patches in some patch families to hotspot patches. For example, the scenario with 11.4%
401 hotspot cover at the watershed scale, required 2.3% of patch families to have two aspatial hotspot
402 patches. Again, this does not mean that there were only one or two hotspots in a patch family,
403 but one or two aspatial patches were used to represent their distribution.

404 Second, we investigated how the saturation status of hotspots influences nitrate export.
405 We built three soil moisture conditions for hotspots by changing the sharing coefficients for local
406 routing which influenced connectivity between hotspot and surrounding patches (Figure 2b): wet
407 (sh_l was 0.05 and sh_g was 0.9 throughout the year; water diffused slowly from hotspots), dry
408 (sh_l and sh_g were set to default values, hotspots diffused water quickly during the dry season),
409 and intermediate (sh_l was 0.1 and sh_g was 0.8 during the dry season but used default values in
410 the wet season; water diffused from hotspots at an intermediate rate). The hotspots in the wet

411 scenario were saturated almost all the time and had small interannual variation in soil moisture.
412 The hotspots in the dry scenario lost water during dry periods and had large interannual soil
413 moisture variation. The hotspots in the intermediate scenario had soil moisture dynamics in
414 between the levels observed in the dry and wet scenarios (Figure 4).

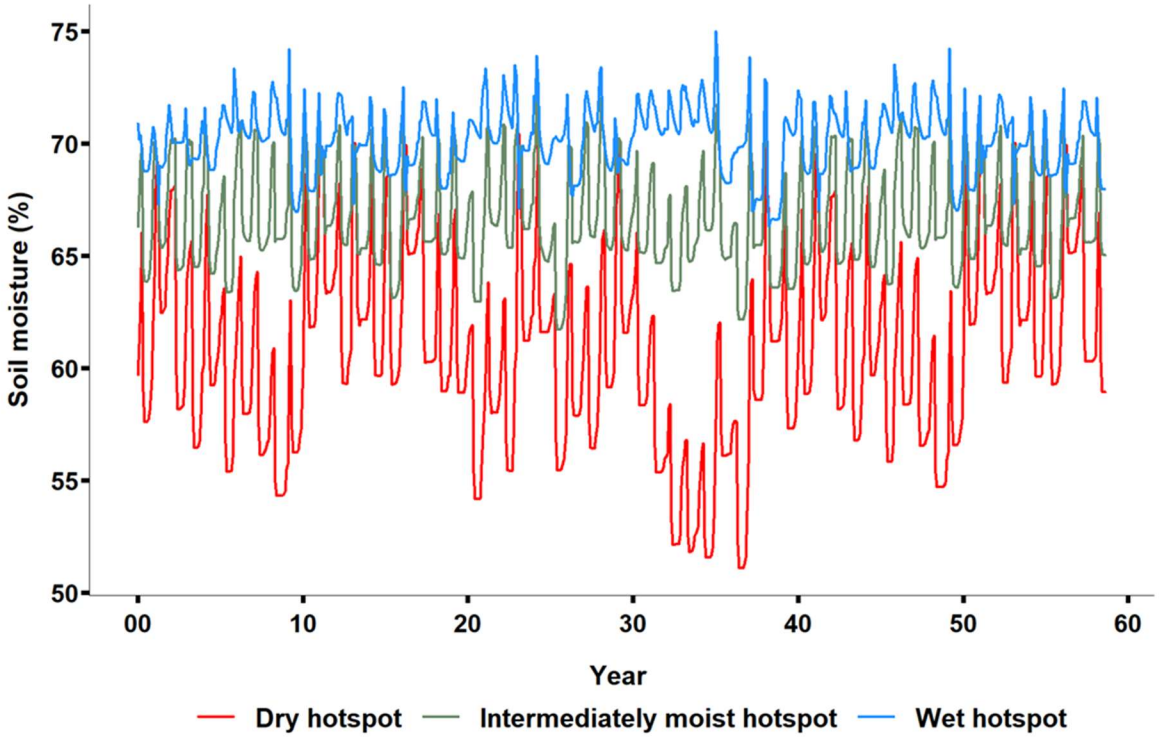

415

416 *Figure 4. Hotspot volumetric soil moisture conditions used to examine the sensitivity of N*
417 *cycling and export to hotspot soil moisture saturation status and timing.*

418 Lastly, we examined how uncertainty in the subsurface connectivity threshold parameter,
419 which determines when non-hotspot patches become reconnected and can receive substantial N
420 and water from the hotspot (θ_{th}; Figure 2c). By establishing conditions for this larger scale
421 connectivity, this parameter can influence streamflow nitrate export. We then compared modeled
422 streamflow nitrate export (under a range of parameter values based on the range of basin scale
423 soil moisture: 0.15, 0.21, 0.25, 0.31, 0.35) to observed data (from 1988 to 2001).

Following the sensitivity analyses, we used available data and literature to estimate the most likely value for these parameters. We selected hotspot abundance of 9.1% assuming every patch family had the same hotspot coverage (using the default value in Table 2). We then selected the "dry" hotspot scenario in order to most closely match the seasonality of N dynamics observed in dryland ecosystems (Parker & Schimel 2011). Finally, as a simple optimization strategy, we selected a value for the soil moisture threshold parameter that enabled us to best capture observed peak N export. Then using these values, we conducted modeling scenarios to investigate how biogeochemical hotspots influence N export.

Modeling scenarios were based on the presence or absence of biogeochemical hotspots. For the hotspot scenario, we used the optimized soil moisture threshold determined using the approach described above, along with default parameters shown in Table 2, which created "dry" hotspots (i.e., with rapid water diffusion) that had distinct seasonality in denitrification as observed in field data (Li et al., 2006; Parker & Schimel, 2011). In this scenario, the hotspot patches received litter and protected C and N from vegetated patches and both biogeochemical and hydrologic processes still occurred within the hotspot patches. For the non-hotspot scenario, we used unvegetated patches in place of the hotspot patches, which were initialized to zero. However, in these unvegetated patches, we did not route litter and recalcitrant soil C and N from the vegetated patches. As a result, only hydrologic processes occurred there. We ran these two scenarios for 120 years, 60 years to stabilize the hotspot patches, and another 60 years to compare differences between scenarios.

3 Results

3.1 Initialization and calibration results

Using the target-driven initialization method of Hanan et al. (2018), we were able to capture the spatial distribution of leaf area index (LAI) and associated C stores across the Bell 4 watershed, with some minor underestimates in riparian areas (covered by live oak) and overestimates in a small percentage of patches, which occurred because RHESSys allocates C to LAI at the end of growing season. Overall, the initialized and remotely sensed LAI were a strong match (Figure S1).

During the calibration period, the monthly NSE (a metric to evaluate the extent to which models capture peak streamflow; values close to 1 represent the best correspondence between modeled and observed values) was 0.88. Percent error (a metric to evaluate total flow; values close to 0 represent low error in the total amount of streamflow for modeled vs. observed data) was 5.45%. For the evaluation period, the monthly NSE was 0.8 with a percent error of -3.92%. In general, the model captured the seasonality, recession, and low flow patterns observed in the streamflow record.

3.2 Sensitivity of N fluxes to the abundance of hotspots

Total N export increased with increasing hotspot cover and then reached an asymptote when hotspot cover was greater than 9.1% (Figure 5). Denitrification rates were very low in the zero percent hotspot cover scenario and increased with an increasing percentage of hotspot patches. However, the rate of increase declined when hotspot cover was greater than 9.1%. Median streamflow nitrate export began increasing when hotspot cover was above 4.5% but reached an asymptote at 9.1%. Maximum streamflow nitrate export also increased with increasing hotspot cover, but the rate of increase declined when cover was above 9.1%. This

occurred because increasing hotspot cover led to concomitant decreases in vegetation cover and therefore less carbon and nitrogen inputs from vegetation to soil. As a result, N cycling processes became limited by productivity of the patch family. Although this result was partly an artifact of the model's structure—which resulted in more than one aspatial hotspot patch occurring in some patch families when the hotspot percentage cover exceeded 9.1%—it still demonstrates the mechanism by which increases in hotspot cover above a given threshold can decrease productivity. However, the actual threshold value should be interpreted with caution.

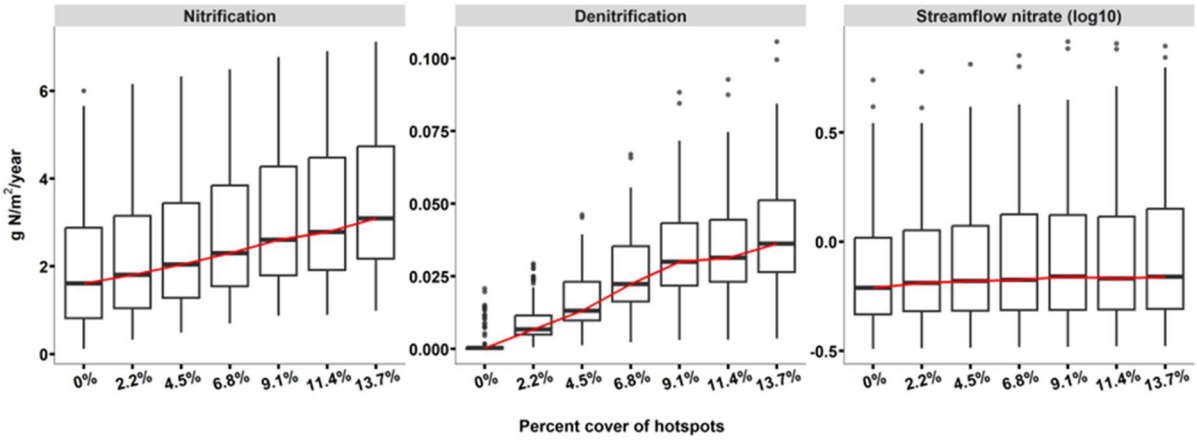

Figure 5. Sensitivity of N processes to the percent cover of hotspots. Box plots show 25th, median, and 75th percentile values, and the red line connects the median of each scenario to show trends. Streamflow nitrate is calculated as total mass of nitrate in discharge divided by the basin area.

3.3 The sensitivity of N fluxes to the parameters controlling water diffusion during periods of hydrologic disconnection.

To examine how the rate at which hotspots dry out during periods of hydrologic disconnection influences N fluxes, we ran three scenarios: a scenario where soil moisture in the hotspots diffused slowly to non-hotspot patches and hotspots retained their soil moisture throughout the year (i.e., a wet hotspot scenario), and a scenario where the diffusion speed was intermediate (i.e., an intermediately moist hotspot scenario), and a scenario where soil moisture

diffused relative quickly from hotspot to non-hotspot patches (i.e., a dry hotspot scenario). We found that basin-scale nitrification rates can increase or decrease with the moisture content of hotspots (Figure 6 b&g). Higher moisture content in hotspots led to relatively lower moisture content in non-hotspot patches (based on water balance). In the wet-hotspot scenario, basin-scale nitrification was lower than in the dry-hotspot scenario where water slowly diffused to non-hotspot patches. This occurred because in the wet-hotspot scenario, soil moisture in non-hotspot patches was lower, which reduced total nitrification, even though nitrification rates increased in the hotspots.

Basin-scale denitrification increased with higher moisture content in hotspots since denitrification mainly occurs in those locations (Figure 6 d&g). For both nitrification and denitrification, the differences between the three scenarios were most pronounced during dry years when soil moisture differences between hotspots and non-hotspot patches were higher (Figure 6 b&d). During dry and average years, streamflow nitrate export was higher in the scenarios where hotspots remained saturated or close to saturated (i.e., the wet- and intermediately-moist- hotspot scenarios) than in the scenario where water diffused rapidly during dry periods (i.e., the dry-hotspot scenario). However, there was higher total annual and peak streamflow nitrate export during the wet years in the dry-hotspot scenario especially after multiple dry years (Figure 6c&e). Altogether, the closer hotspots are to being water-saturated, the more quickly N is exported to streamflow.

During multiple dry years, for the rapid diffusion (dry hotspot) scenario, nitrate accumulated in the saturated zone. Once a wet year occurred, that nitrate was flushed out to streams (Figure 6a). In the more continuously saturated (wet hotspot) hotspot scenario, higher denitrification, and faster leaching of nitrate from hotspots led to less nitrate accumulation in the

saturated zone. This suggests that soil moisture in hotspots and the subsurface flow interact to drive N movement from soil to streams.

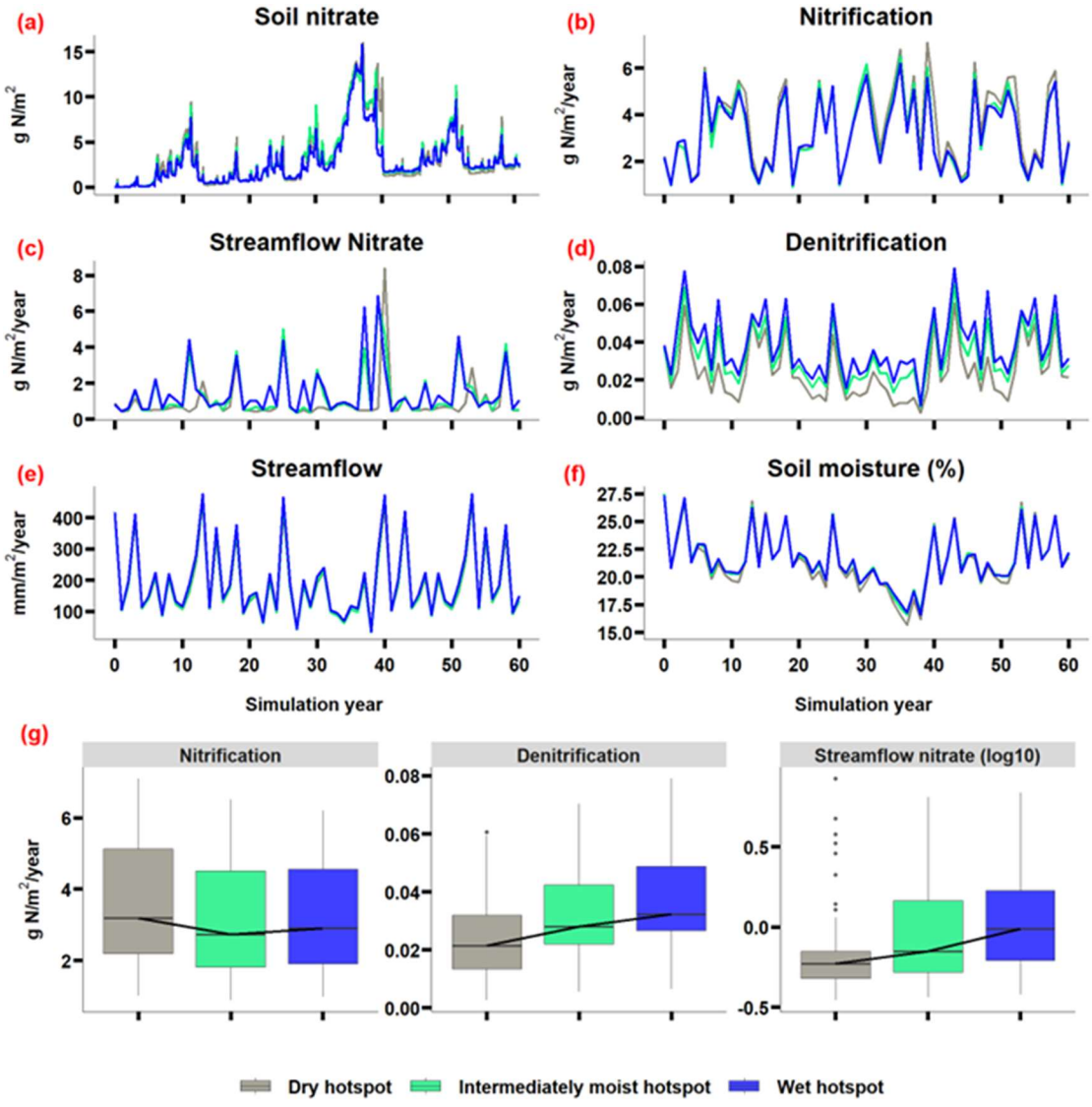

Figure 6. N processes for three different scenarios, one where hotspots were saturated most of the time (i.e., the slow diffusion, wet hotspot scenario), one where water diffused more rapidly from hotspots during the dry season (i.e., the rapid diffusion, dry hotspot scenario), and one where diffusion was intermediate (i.e., the intermediately moist hotspot scenario). Streamflow is calculated as the average water depth over the basin area of Bell 4 (0.14 km^2). Panel (g) is the distribution of annual N fluxes, box plots show 25th, median, 75th percentile, and the black line connects the median of each scenario.

519 **3.4 Sensitivity of N export to the subsurface connectivity parameter**

520 The soil moisture threshold, which controls the connectivity of hotspots to non-hotspot
521 patches, had a stronger influence on streamflow nitrate export than on nitrification and
522 denitrification fluxes (Figure 7). This occurred because streamflow N export is influenced by
523 both soil moisture content and subsurface lateral transport. Thus, when the threshold was high
524 (i.e., when more moisture was required to establish hydrologic connectivity), streamflow N
525 export was close to zero. With a higher soil moisture threshold, hotspots also tended to have
526 higher moisture content, which increased nitrification and denitrification (Figure 7e), although
527 the increases were small. The soil moisture threshold affected both the magnitude and timing of
528 streamflow nitrate export. At a very low threshold of 0.15, there was higher magnitude and
529 similar timing of peak nitrate export to streams compared to the no-threshold scenario (fully
530 connected). This occurred because soil moisture in non-hotspot patches was higher than 0.15
531 most of the time (Figure 7d). A threshold of 0.21, which was around the median basin-scale soil
532 moisture, caused the largest peak in streamflow nitrate export. This occurred because
533 connectivity was delayed until the threshold was reached, allowing nitrate to accumulate. When
534 the threshold was larger than 0.21, peak streamflow nitrate was smaller and came later because
535 hotspots were disconnected from non-hotspot patches most of the time.

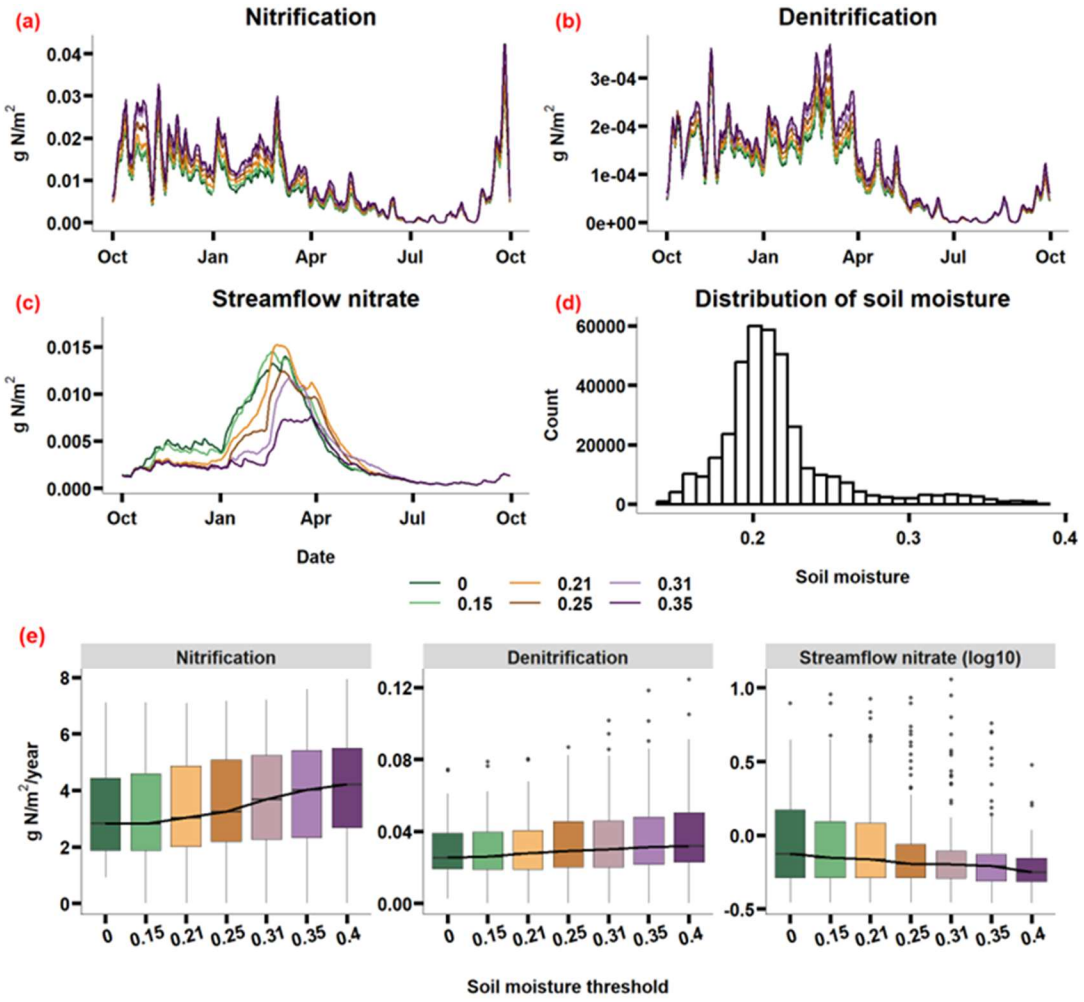

Figure 7. *Sensitivity of N fluxes to the soil moisture threshold. Panels (a), (b) and (c) are mean daily N fluxes over 60 years. Panel (d) is the distribution of daily soil moisture at the basin scale over 60 years. Panel (e) is the distribution of annual fluxes, box plots show 25th, median, 75th percentile, and the black line connects the median of each scenario. Different colors represent different soil moisture thresholds.*

3.5 Prediction of streamflow N export compared with observations.

We selected the optimal soil moisture threshold from section 3.2 for capturing the magnitude of observed nitrate export (i.e., 0.21; this parameter value maximized peak streamflow nitrate export) and we used the default values shown in Table 2 for the other parameters. Using these values, we found that hydrologic disconnection of soil hotspots during the dry periods and reconnection during wet periods enabled us to capture the observed

magnitude of nitrate export in streamflow, which we could not otherwise capture in the non-hotspot scenario (Figure 8). For example, the non-hotspot scenario underestimated nitrate export with a NSE of 0.22, while the hotspot scenario increased the estimation peak streamflow nitrate by 29% and captured its timing better with a NSE of 0.4 (in 1988, 1991, 1992, 1993, 2000). However, after optimizing the moisture threshold parameter, the timing of stream nitrate export was still slightly off; for example, in 1998, the modeled stream nitrate export peak was higher and occurred slightly later than observed.

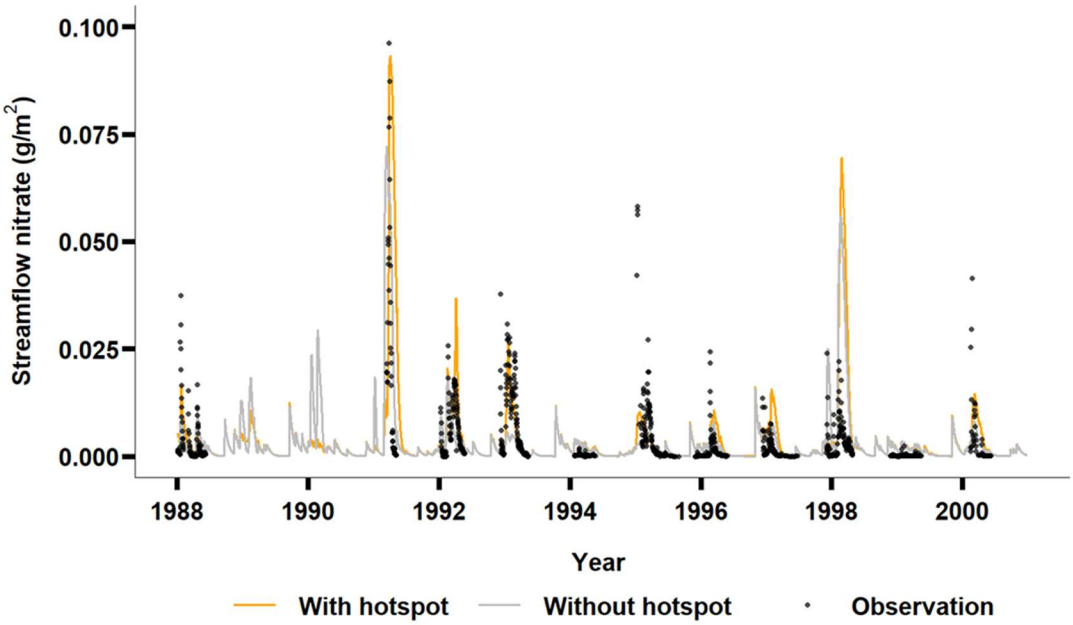

Figure 8. Simulated and observed nitrate export in streamflow. The dots show observed streamflow nitrate.

3.6 Comparison of hotspot and non-hotspot scenarios

At the basin-scale, there was higher N export in the hotspot scenario than in the non-hotspot scenario (Figure 9). Increases in streamflow nitrate with the hotspot scenario closely corresponded with increases in soil nitrate. Nitrate accumulated during dry years and there was substantial nitrate export to streams in wet years, especially when a wet year followed multiple

dry years (e.g., in year 40). We also found that streamflow nitrate export was further influenced by interannual precipitation patterns. The differences between the hotspot and non-hotspot scenarios were most evident during wet years when the basin was more connected. During wet years, more nitrate was flushed out from hotspots, which illustrates how subsurface connectivity can be an important factor driving streamflow N export. Consequently, the differences in streamflow nitrate between the hotspot and non-hotspot scenarios were less consistent than the differences in nitrification and denitrification, which had similar temporal patterns but differing magnitude (e.g., Figure 9 c&d).

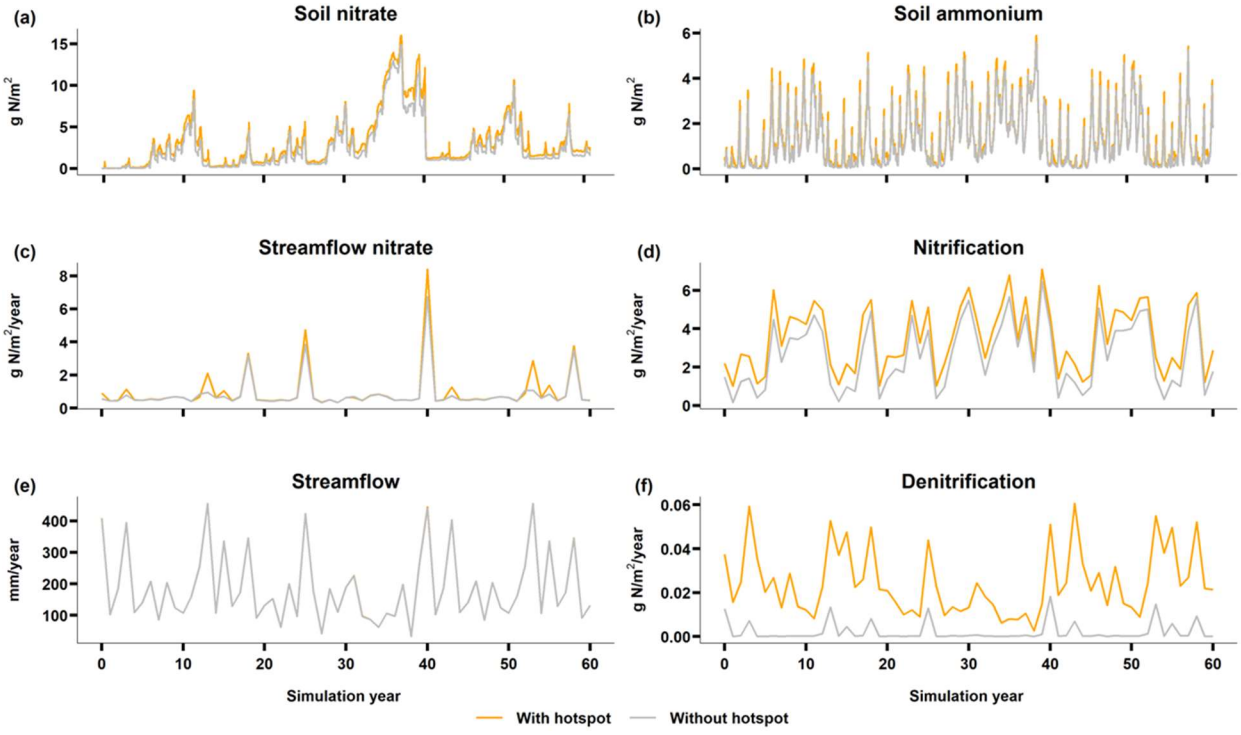

Figure 9. Nitrogen and hydrologic cycling processes (annual sum) and nitrate pools (annual mean) at the full basin scale for Bell 4.

4 Discussion

Modeling hotspots at watershed scales has been challenging because most models, including RHESSys, lack corresponding fine-scale (e.g., below 1-meter resolution) parameters

and variables (Tague, 2009). To address this limitation, we developed a framework for representing hotspots aspatially within 10-m resolution patches. Using this framework, we conducted a series of virtual experiments to investigate how uncertainties in model structure and parameters influence N cycling and export. Then using the new modeling framework, we examined how precipitation can affect N export in a dryland watershed in California. Our model framework and virtual experiments improve our ability to connect plot-scale measurements to catchment scale projections by developing integrative model algorithms and parameters that control the biophysical behavior of hotspots across a landscape. These parameters can be optimized using field observations of N cycling and export. We illustrate how uncertainty in model parameters can influence projections of N export. Future research should aim to reduce these uncertainties, and ultimately represent hotspot behavior more mechanistically across watersheds.

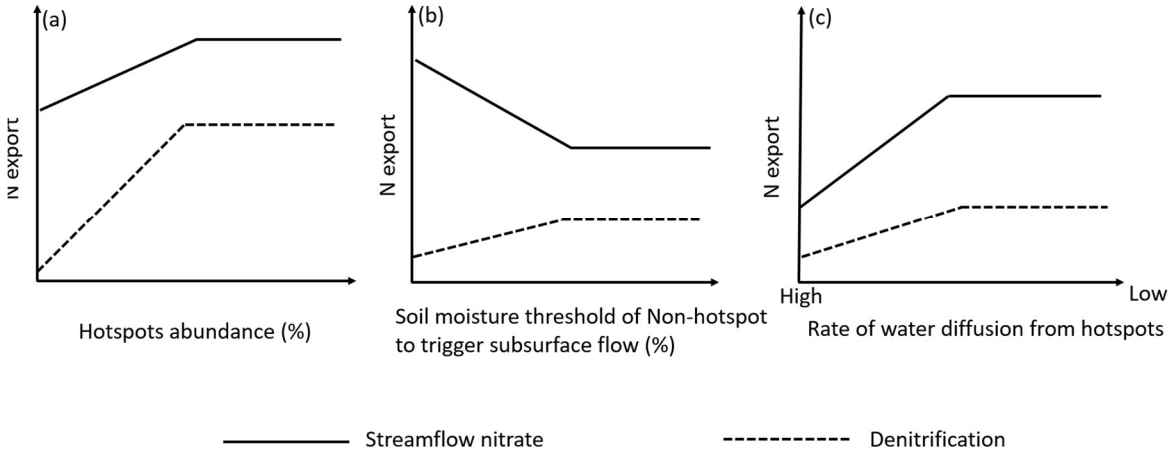

Figure 10. Conceptual framework summarizing how total annual streamflow nitrate and denitrification respond to (a) hotspots abundance, (b) the soil moisture threshold required to trigger subsurface flow, and (c) the rate of water diffusion from hotspots.

4.1. Uncertainties related to hotspot abundance and distribution

Estimating nitrogen (N) export at watershed and regional scales is limited by uncertainty in how hotspots are distributed across landscapes. Our research is among the few studies that have evaluated how hotspot abundance influences watershed-scale N export and illustrates the need to quantify hotspot cover to effectively scale N dynamics from ecosystems to watersheds (Anderson et al., 2015; Groffman, 2012). We parameterized the hotspots with varying cover percentages across a small watershed (0.14 km^2) and found that N export increased with hotspot abundance (Figure 5& Figure 10), but with an asymptotic relationship due to limitations in N inputs and plant productivity (i.e., energy input for denitrification). However, in less N-limited and more mesic sites (e.g., under elevated N deposition and increasing precipitation), N export may be more sensitive to increasing hotspot abundance.

One limitation of our study is that we did not examine how the spatial distribution of hotspots influences N export. Previous research has shown that hotspots can be more concentrated in riparian corridors and wetlands where moisture content is higher (Pinay et al., 2015). We did however find that wet hotspots, which may serve as a surrogate for riparian and wetland locations, can in some cases increase both denitrification and N export in streams (Figure 6). However, because the location and arrangement of hotspots across a landscape can significantly influence streamflow N export (Laudon et al., 2011; Pinay et al., 2015), more research is needed to understand these spatial relationships (Haas et al., 2013). For example, combing high-resolution remote sensing data with field observations may help us better constrain hotspot distribution and abundance in ecohydrological models (Goodridge et al., 2018; Groffman, 2012; Tague, 2009; Walter et al., 2000).

615 **4.2 Uncertainties in how rapidly hotspots dry out**

616 Soil moisture is a major factor regulating denitrification and streamflow nitrate export
617 (Pinay et al., 2015; Zhu et al., 2012). Our modeling experiments illustrate how the relationships
618 between soil moisture and N dynamics can be complex and non-linear. Elevated soil moisture
619 may reduce nitrification, increase denitrification, and ultimately decrease the amount of nitrate
620 available for hydrologic flushing. Drier soils on the other hand can decrease denitrification and
621 increase the amount of nitrate available for flushing (Homyak et al., 2016). We found that during
622 dry and average years, higher moisture in hotspots increased nitrate infiltration from the
623 unsaturated zone to the saturated zone, resulting in elevated and more rapid nitrate export to
624 streams (Figure 6c). However, during wet years, higher soil moisture led to less nitrate export to
625 streams due to increases in denitrification combined with less nitrate in the subsurface from the
626 legacy effects of leaching in prior average and dry years. The dry hotspot scenario captured the
627 observed nitrate-flushing better than the wet scenario, suggesting that hotspots are not likely to
628 be continuously saturated (Figure 6). Because recent studies have shown that very small changes
629 in soil moisture can change N fluxes abruptly (Castellano et al., 2013; Evans et al., 2016), it is
630 important to improve our representation of soil moisture conditions in hotspots to accurately
631 predict nitrate export.

632 Soil water residence time is an important factor affecting N export (Pinay et al., 2015;
633 Zarnetske et al., 2011). The slower water diffuses from hotspots, the longer nitrate is exposed to
634 denitrifying conditions (McClain et al., 2003). Our study shows that longer water residence time
635 in hotspots (i.e., in the wet hotspot scenario) increases both denitrification and total N export to
636 streams (Figure 6 & Figure 10). We used water diffusion coefficients to model water residence
637 time in hotspots and we selected coefficients that enabled us to best capture the plausible timing

638 of denitrification and streamflow N fluxes. While this is a simplified, proxy approach, adding
639 further complexity by explicitly modeling diffusion maybe infeasible since it would require
640 local, spatially explicit soil parameters (Wood et al., 2011). However, further investigation into
641 how proxy parameters may be calibrated is recommended for future research.

642 Stream nitrate export was also affected by precipitation patterns. When there were
643 multiple dry years in a row, nitrate accumulated to a greater extent than in average years (Figure
644 6a). When a wet year followed a multi-year drought, there was higher streamflow nitrate export
645 in the dry hotspot scenario (Figure 6c). This is corroborated by field observations, which suggest
646 that severe drought promoted nitrate accumulation in soil due to less denitrification and plant
647 uptake, resulting in more nitrate available for flushing with the return of precipitation (Winter et
648 al. 2023). We found that the length of drought and precipitation variability were more important
649 in driving streamflow N export than the amount of precipitation (Figure 6c&e). For example,
650 even with similar amount of precipitation in simulation years 26 and 40, N export was much
651 higher in year 40 due to the legacy of a multi-year drought (Figure 6c&e). Recent research has
652 similarly shown that precipitation variability can have positive or negative legacy effects on
653 dryland productivity, which can in turn influence N cycling and export (Gherardi & Sala, 2015;
654 Krichels et al., 2022). However, the direction of N responses vary along long-term precipitation
655 gradients (Gherardi & Sala, 2015, 2019).

656 **4.3 Uncertainties in hydrologic connectivity**

657 The subsurface flow threshold also plays a role in how much nitrate is transported to
658 streams. In this study, we found that the optimal volumetric soil moisture to trigger subsurface
659 flow from hotspot to non-hotspot patches was around 21% (Figure 7). Other studies have
660 similarly shown that to trigger a subsurface flow, the soil moisture needs to reach a threshold of

18% (Liao et al., 2016). However, this threshold may vary with soil texture and water potential dynamics. While our new model framework can improve the prediction of streamflow nitrate with a static soil moisture threshold, topography and vegetation cover can also influence the connectivity and amount of subsurface flow, suggesting that soil moisture thresholds should be dynamic (Crow et al., 2012, Zhu et al., 2018).

Coupling soil biogeochemical models with hydrological models has become increasingly popular for investigating N cycling and export (Schimel, 2018). To save time, researchers typically prefer to couple existing models rather than build new ones (Malek et al., 2017; Zhu et al., 2018). Since most hydrologic models do not account for fine-scale heterogeneity in available moisture, they may not be able to capture biogeochemical hotspots even when coupled with biogeochemical models (Chen et al., 2020). Our new model framework provides a relatively simple way to capture hotspots without having to explicitly represent sub-meter scale spatial heterogeneity. While this intermediate complexity approach enables us to represent hotspots across a watershed, it does not fully capture some of the potential controls on hotspot function. For example, although our model captured the variability and magnitude of streamflow nitrate, there was some error associated with its timing (Figure 8). Future work can build upon our simple hotspot model to develop more process-based and dynamic representation of subsurface flow thresholds. This can be achieved by improving our understanding of hydrology and N processes in soil through hydrogeochemical observations.

4.4 The role of hotspots and hot moments in watershed models

We found that the catchment-scale denitrification rate in the hotspot scenarios was significantly higher than that observed in the non-hotspot scenario (Figure 5& Figure 9), aligning with the concept that small areas often account for a high percentage of denitrification activity

(McClain et al., 2003). Additionally, denitrification was more sensitive to hotspot abundance, while N export to streams was more sensitive to the soil moisture threshold that triggers subsurface flow (Figure 10). Both are affected by the speed at which water diffuses from hotspots, which influences soil moisture levels, water residence time in soil, and vertical and horizontal transport of water. Our virtual experiments provide information on model uncertainty and sensitivity that can inform future studies focused on scaling N processes from plots to catchments. For example, in areas with high N deposition, managers who are interested in predicting how much N ends up in streams should focus on reducing model uncertainties in subsurface flow thresholds and soil moisture retention in hotspots.

In the context of predicting N export, hot moments—defined as wet periods after a prolonged dry spell (Groffman et al., 2009)—are currently better represented in the RHESSys model than hotspots. Even in our no hotspot scenario, there was a pulse of streamflow N export when wet years followed multiple dry years (Figure 6 & Figure 9). However, models of how hot moments influence streamflow N export are still limited by uncertainties in soil moisture dynamics. For instance, we found that in the wet hotspot scenario, there was an earlier streamflow N pulse than in the dry hotspot scenario (Figure 6c). Thus, hotspot conditions can affect the timing of hot moments, which has not been previously explored in modeling studies. In future studies, it is important to consider interactions between hotspots and hot moments rather than discussing them in isolation.

5 Conclusion

Coupling hydrologic processes with biogeochemical processes in watershed-scale models is challenging due to subsurface heterogeneity and the existence of hotspots and hot moments that are not well represented in models. We developed a framework for representing hotspots

explicitly in dryland watersheds and using this framework, we demonstrated how hydrologic connectivity and precipitation can affect N export in a dryland watershed in California. With increasing hotspot coverage (up to a threshold), both denitrification and N export to streams increased. The partitioning between denitrification and N-export, and the timing and magnitude of N-export were largely controlled by hotspot soil moisture dynamics. Specifically, we found that when the soil moisture threshold required for reestablishing subsurface flow was intermediate, nitrate was able to accumulate during drier periods and then be flushed to the stream upon wet up. This led to the highest peak nitrate export to streams, which tended to better-capture observed nitrate patterns. To our knowledge, this is the first time biogeochemical hotspots have been modeled explicitly using a coupled biogeochemical-ecohydrological model in a dryland watershed. This modeling framework can help better project N export in dryland watersheds where hotspots may play an increasingly important role in governing water quality as drought and N deposition continue to increase.

6 Acknowledgments

This project was supported by National Science Foundation of the United States under award number DEB-1916658. We thank Tom Dilts for helping with preparing input maps and data of RHESSys. We thank Pete Wohlgemuth for helping with streamflow data processing and model calibration. This study was supported in part by the USDA Forest Service Rocky Mountain Research Station. The findings and conclusions in this publication are those of the author and should not be construed to represent any official USDA or U.S. Government determination or policy.

Conflict of Interest

The authors declare no conflicts of interest relevant to this study.

Data Availability Statement

The data sets used to run simulations for this study can be found in the Open Science Forum: https://osf.io/ukpjg/, and the model code can be found on GitHub: https://doi.org/10.5281/zenodo.7754375.

References

Abatzoglou, J. T. (2013). Development of gridded surface meteorological data for ecological applications and modelling. *International Journal of Climatology*, *33*(1), 121–131. https://doi.org/10.1002/joc.3413

Anderson, T. R., Groffman, P. M., & Walter, M. T. (2015). Using a soil topographic index to distribute denitrification fluxes across a northeastern headwater catchment. *Journal of Hydrology*, *522*, 123–134. https://doi.org/10.1016/j.jhydrol.2014.12.043

Baret, F., Olioso, A., Luciani, J. L., Hanocq, J. F., & Monterrot, J. C. (1989). Estimation à partir de mesures de réflectance spectrale du rayonnement photosynthétiquement actif absorbé par une culture de blé. *Agronomie*, *9*(9), 885–895. https://doi.org/10.1051/agro:19890906

Borer, E. T., & Stevens, C. J. (2022). Nitrogen deposition and climate: an integrated synthesis. *Trends in Ecology & Evolution*. https://doi.org/10.1016/j.tree.2022.02.013

Burke, W. D., Tague, C., Kennedy, M. C., & Moritz, M. A. (2021). Understanding How Fuel Treatments Interact With Climate and Biophysical Setting to Affect Fire, Water, and Forest Health: A Process-Based Modeling Approach. *Frontiers in Forests and Global Change*, *3*. https://doi.org/10.3389/ffgc.2020.591162

Castellano, M. J., Lewis, D. B., & Kaye, J. P. (2013). Response of soil nitrogen retention to the interactive effects of soil texture, hydrology, and organic matter. *Journal of Geophysical Research: Biogeosciences*, *118*(1), 280–290. https://doi.org/10.1002/jgrg.20015

Chaney, N. W., Wood, E. F., McBratney, A. B., Hempel, J. W., Nauman, T. W., Brungard, C. W., & Odgers, N. P. (2016). POLARIS: A 30-meter probabilistic soil series map of the contiguous United States. *Geoderma*, *274*, 54–67. https://doi.org/10.1016/j.geoderma.2016.03.025

Chen, X., Tague, C. L., Melack, J. M., & Keller, A. A. (2020). Sensitivity of nitrate concentration-discharge patterns to soil nitrate distribution and drainage properties in the vertical dimension. *Hydrological Processes*, *34*(11), 2477–2493. https://doi.org/10.1002/hyp.13742

Clark, M. P., Bierkens, M. F. P., Samaniego, L., Woods, R. A., Uijlenhoet, R., Bennett, K. E., et al. (2017). The evolution of process-based hydrologic models: historical challenges and the collective quest for physical realism. *Hydrology and Earth System Sciences*, *21*(7), 3427–3440. https://doi.org/10.5194/hess-21-3427-2017

Crow, W. T., Berg, A. A., Cosh, M. H., Loew, A., Mohanty, B. P., Panciera, R., et al. (2012). Upscaling sparse ground-based soil moisture observations for the validation of coarse-resolution satellite soil moisture products. *Reviews of Geophysics*, *50*(2). https://doi.org/10.1029/2011RG000372

Dunn, P. H., Barro, S. C., Wells, W. G., Poth, M. A., Wohlgemuth, P. M., & Colver, C. G. (1988). *The San Dimas experimental forest: 50 years of research* (No. PSW-GTR-104) (p. PSW-GTR-104). Berkeley, CA: U.S. Department of Agriculture, Forest Service,

772 Pacific Southwest Forest and Range Experiment Station. https://doi.org/10.2737/PSW-
773 GTR-104
774 Eagleson, P. S. (1978). Climate, soil, and vegetation: 3. A simplified model of soil moisture
775 movement in the liquid phase. *Water Resources Research*, *14*(5), 722–730.
776 https://doi.org/10.1029/WR014i005p00722
777 Ebrahimi, A., & Or, D. (2018). On Upscaling of Soil Microbial Processes and Biogeochemical
778 Fluxes From Aggregates to Landscapes. *Journal of Geophysical Research:*
779 *Biogeosciences*, *123*(5), 1526–1547. https://doi.org/10.1029/2017JG004347
780 Evans, S., Dieckmann, U., Franklin, O., & Kaiser, C. (2016). Synergistic effects of diffusion and
781 microbial physiology reproduce the Birch effect in a micro-scale model. *Soil Biology and*
782 *Biochemistry*, *93*, 28–37. https://doi.org/10.1016/j.soilbio.2015.10.020
783 Fenn, M. E., Baron, J. S., Allen, E. B., Rueth, H. M., Nydick, K. R., Geiser, L., et al. (2003).
784 Ecological Effects of Nitrogen Deposition in the Western United States. *BioScience*,
785 *53*(4), 404–420. https://doi.org/10.1641/0006-3568(2003)053[0404:EEONDI]2.0.CO;2
786 Gherardi, L. A., & Sala, O. E. (2015). Enhanced precipitation variability decreases grass- and
787 increases shrub-productivity. *Proceedings of the National Academy of Sciences*, *112*(41),
788 12735–12740. https://doi.org/10.1073/pnas.1506433112
789 Gherardi, L. A., & Sala, O. E. (2019). Effect of interannual precipitation variability on dryland
790 productivity: A global synthesis. *Global Change Biology*, *25*(1), 269–276.
791 https://doi.org/10.1111/gcb.14480
792 Goodridge, B. M., Hanan, E. J., Aguilera, R., Wetherley, E. B., Chen, Y.-J., D'Antonio, C. M.,
793 & Melack, J. M. (2018). Retention of Nitrogen Following Wildfire in a Chaparral
794 Ecosystem. *Ecosystems*, *21*(8), 1608–1622. https://doi.org/10.1007/s10021-018-0243-3

795 Groffman, P. M. (2012). Terrestrial denitrification: challenges and opportunities. *Ecological*
796 *Processes*, *1*(1), 1–11. https://doi.org/10.1186/2192-1709-1-11
797 Groffman, P. M., Butterbach-Bahl, K., Fulweiler, R. W., Gold, A. J., Morse, J. L., Stander, E. K.,
798 et al. (2009). Challenges to incorporating spatially and temporally explicit phenomena
799 (hotspots and hot moments) in denitrification models. *Biogeochemistry*, *93*(1–2), 49–77.
800 https://doi.org/10.1007/s10533-008-9277-5
801 Gustine, R. N., Hanan, E. J., Robichaud, P. R., & Elliot, W. J. (2022). From burned slopes to
802 streams: how wildfire affects nitrogen cycling and retention in forests and fire-prone
803 watersheds. *Biogeochemistry*, *157*(1), 51–68. https://doi.org/10.1007/s10533-021-00861-
804 0
805 Haas, E., Klatt, S., Fröhlich, A., Kraft, P., Werner, C., Kiese, R., et al. (2013). LandscapeDNDC:
806 a process model for simulation of biosphere–atmosphere–hydrosphere exchange
807 processes at site and regional scale. *Landscape Ecology*, *28*(4), 615–636.
808 https://doi.org/10.1007/s10980-012-9772-x
809 Hanan, E. J., Tague, C. (Naomi), & Schimel, J. P. (2017). Nitrogen cycling and export in
810 California chaparral: the role of climate in shaping ecosystem responses to fire.
811 *Ecological Monographs*, *87*(1), 76–90. https://doi.org/10.1002/ecm.1234
812 Hanan, E. J., Tague, C., Choate, J., Liu, M., Kolden, C., & Adam, J. (2018). Accounting for
813 disturbance history in models: using remote sensing to constrain carbon and nitrogen pool
814 spin-up. *Ecological Applications: A Publication of the Ecological Society of America*,
815 *28*(5), 1197–1214. https://doi.org/10.1002/eap.1718
816 Hanan, E. J., Ren, J., Tague, C. L., Kolden, C. A., Abatzoglou, J. T., Bart, R. R., et al. (2021).
817 How climate change and fire exclusion drive wildfire regimes at actionable scales.

Environmental Research Letters, *16*(2), 024051. https://doi.org/10.1088/1748-9326/abd78e

Hartigan, J. A., & Wong, M. A. (1979). Algorithm AS 136: A K-Means Clustering Algorithm. *Journal of the Royal Statistical Society. Series C (Applied Statistics)*, *28*(1), 100–108. https://doi.org/10.2307/2346830

Homyak, P. M., Sickman, J. O., Miller, A. E., Melack, J. M., Meixner, T., & Schimel, J. P. (2014). Assessing Nitrogen-Saturation in a Seasonally Dry Chaparral Watershed: Limitations of Traditional Indicators of N-Saturation. *Ecosystems*, *17*(7), 1286–1305. https://doi.org/10.1007/s10021-014-9792-2

Homyak, P. M., Blankinship, J. C., Marchus, K., Lucero, D. M., Sickman, J. O., & Schimel, J. P. (2016). Aridity and plant uptake interact to make dryland soils hotspots for nitric oxide (NO) emissions. *Proceedings of the National Academy of Sciences*, *113*(19), E2608–E2616. https://doi.org/10.1073/pnas.1520496113

Krichels, A. H., Greene, A. C., Jenerette, G. D., Spasojevic, M. J., Glassman, S. I., & Homyak, P. M. (2022). Precipitation legacies amplify ecosystem nitrogen losses from nitric oxide emissions in a Pinyon–Juniper dryland. *Ecology*, *n/a*(n/a), e3930. https://doi.org/10.1002/ecy.3930

Laudon, H., Berggren, M., Ågren, A., Buffam, I., Bishop, K., Grabs, T., et al. (2011). Patterns and Dynamics of Dissolved Organic Carbon (DOC) in Boreal Streams: The Role of Processes, Connectivity, and Scaling. *Ecosystems*, *14*(6), 880–893. https://doi.org/10.1007/s10021-011-9452-8

Li, X., Meixner, T., Sickman, J. O., Miller, A. E., Schimel, J. P., & Melack, J. M. (2006). Decadal-scale Dynamics of Water, Carbon and Nitrogen in a California Chaparral

841 Ecosystem: DAYCENT Modeling Results. *Biogeochemistry*, *77*(2), 217–245.
842 https://doi.org/10.1007/s10533-005-1391-z
843 Liao, K.-H., Lv, L.-G., Yang, G.-S., & Zhu, Q. (2016). Sensitivity of simulated hillslope
844 subsurface flow to rainfall patterns, soil texture and land use. *Soil Use and Management*,
845 *32*(3), 422–432. https://doi.org/10.1111/sum.12282
846 Lin, L., Webster, J. R., Hwang, T., & Band, L. E. (2015). Effects of lateral nitrate flux and
847 instream processes on dissolved inorganic nitrogen export in a forested catchment: A
848 model sensitivity analysis. *Water Resources Research*, *51*(4), 2680–2695.
849 https://doi.org/10.1002/2014WR015962
850 Malek, K., Stöckle, C., Chinnayakanahalli, K., Nelson, R., Liu, M., Rajagopalan, K., et al.
851 (2017). VIC–CropSyst-v2: A regional-scale modeling platform to simulate the nexus of
852 climate, hydrology, cropping systems, and human decisions. *Geoscientific Model*
853 *Development*, *10*(8), 3059–3084. https://doi.org/10.5194/gmd-10-3059-2017
854 Maxwell, A. E., Warner, T. A., Vanderbilt, B. C., & Ramezan, C. A. (2017). Land Cover
855 Classification and Feature Extraction from National Agriculture Imagery Program
856 (NAIP) Orthoimagery: A Review. *Photogrammetric Engineering & Remote Sensing*,
857 *83*(11), 737–747. https://doi.org/10.14358/PERS.83.10.737
858 McClain, M. E., Boyer, E. W., Dent, C. L., Gergel, S. E., Grimm, N. B., Groffman, P. M., et al.
859 (2003). Biogeochemical Hot Spots and Hot Moments at the Interface of Terrestrial and
860 Aquatic Ecosystems. *Ecosystems*, *6*(4), 301–312. https://doi.org/10.1007/s10021-003-
861 0161-9

862 Meentemeyer, R. K., & Moody, A. (2002). Distribution of plant life history types in California
863 chaparral: the role of topographically-determined drought severity. *Journal of Vegetation*
864 *Science*, *13*(1), 67–78. https://doi.org/10.1111/j.1654-1103.2002.tb02024.x
865 Meixner, T., Fenn, M. E., Wohlgemuth, P., Oxford, M., & Riggan, P. (2006). N Saturation
866 Symptoms in Chaparral Catchments Are Not Reversed by Prescribed Fire. *Environmental*
867 *Science & Technology*, *40*(9), 2887–2894. https://doi.org/10.1021/es051268z
868 Nash, J. E., & Sutcliffe, J. V. (1970). River flow forecasting through conceptual models part I —
869 A discussion of principles. *Journal of Hydrology*, *10*(3), 282–290.
870 https://doi.org/10.1016/0022-1694(70)90255-6
871 Osborne, B. B., Nasto, M. K., Soper, F. M., Asner, G. P., Balzotti, C. S., Cleveland, C. C., et al.
872 (2020). Leaf litter inputs reinforce islands of nitrogen fertility in a lowland tropical forest.
873 *Biogeochemistry*, *147*(3), 293–306. https://doi.org/10.1007/s10533-020-00643-0
874 Ouyang, W., Xu, X., Hao, Z., & Gao, X. (2017). Effects of soil moisture content on upland
875 nitrogen loss. *Journal of Hydrology*, *546*, 71–80.
876 https://doi.org/10.1016/j.jhydrol.2016.12.053
877 Parker, S. S., & Schimel, J. P. (2011). Soil nitrogen availability and transformations differ
878 between the summer and the growing season in a California grassland. *Applied Soil*
879 *Ecology*, *48*(2), 185–192. https://doi.org/10.1016/j.apsoil.2011.03.007
880 Parton, W. J. (1996). The CENTURY model. In D. S. Powlson, P. Smith, & J. U. Smith (Eds.),
881 *Evaluation of Soil Organic Matter Models* (Vol. 38, pp. 283–291). Springer, Berlin,
882 Heidelberg: Evaluation of Soil Organic Matter Models.
883 Phillip, J. (1957). The theory of infiltration: 4. Sorptivity and algebraic infiltration equation. *Soil*
884 *Sci*, *84*, 257–264.

885 Pinay, G., Peiffer, S., De Dreuzy, J.-R., Krause, S., Hannah, D. M., Fleckenstein, J. H., et al.
886 (2015). Upscaling Nitrogen Removal Capacity from Local Hotspots to Low Stream
887 Orders' Drainage Basins. *Ecosystems*, *18*(6), 1101–1120. https://doi.org/10.1007/s10021-
888 015-9878-5
889 Poblador, S., Lupon, A., Sabaté, S., & Sabater, F. (2017). Soil water content drives
890 spatiotemporal patterns of CO_2 and N_2O emissions from a Mediterranean riparian forest
891 soil. *Biogeosciences*, *14*(18), 4195–4208. https://doi.org/10.5194/bg-14-4195-2017
892 R Core Team. (2022). R: A Language and Environment for Statistical Computing. Retrieved
893 from https://www.R-project.org/
894 Ren, J., Adam, J. C., Hicke, J. A., Hanan, E. J., Tague, C. L., Liu, M., et al. (2021). How does
895 water yield respond to mountain pine beetle infestation in a semiarid forest? *Hydrology*
896 *and Earth System Sciences*, *25*(9), 4681–4699. https://doi.org/10.5194/hess-25-4681-
897 2021
898 Ren, J., Hanan, E., Hicke, J., Kolden, C., Abatzoglou, J. T., Tague, C., et al. (2022, March 23).
899 Bark beetle effects on fire regimes depend on underlying fuel modifications in semiarid
900 systems [preprint]. https://doi.org/10.1002/essoar.10510802.1
901 Ridolfi, L., Laio, F., & D'Odorico, P. (2008). Fertility Island Formation and Evolution in
902 Dryland Ecosystems. *Ecology and Society*, *13*(1). https://doi.org/10.5751/ES-02302-
903 130105
904 Schimel, J. P. (2018). Life in Dry Soils: Effects of Drought on Soil Microbial Communities and
905 Processes. *Annual Review of Ecology, Evolution, and Systematics*, *49*(1), 409–432.
906 https://doi.org/10.1146/annurev-ecolsys-110617-062614

907 Schmidt, J. P., Hong, N., Dellinger, A., Beegle, D. B., & Lin, H. (2007). Hillslope Variability in
908 Corn Response to Nitrogen Linked to In-Season Soil Moisture Redistribution. *Agronomy*
909 *Journal*, *99*(1), 229–237. https://doi.org/10.2134/agronj2006.0187
910 Seager, R., Lis, N., Feldman, J., Ting, M., Williams, A. P., Nakamura, J., et al. (2018). Whither
911 the 100th Meridian? The Once and Future Physical and Human Geography of America's
912 Arid–Humid Divide. Part I: The Story So Far. *Earth Interactions*, *22*(5), 1–22.
913 https://doi.org/10.1175/EI-D-17-0011.1
914 Smith, F. W., Sampson, D. A., & Long, J. N. (1991). Comparison of Leaf Area Index Estimates
915 from Tree Allometrics and Measured Light Interception. *Forest Science*, *37*(6), 1682–
916 1688. https://doi.org/10.1093/forestscience/37.6.1682
917 Soil Survey Staff. (2022). *Keys to Soil Taxonomy, 13th ed.* USDA-Natural Resources.
918 Tague, C. (2009). Modeling hydrologic controls on denitrification: sensitivity to parameter
919 uncertainty and landscape representation. *Biogeochemistry*, *93*(1/2,), 79–90.
920 Tague, C. L., & Band, L. E. (2004). RHESSys: Regional Hydro-Ecologic Simulation System—
921 An Object-Oriented Approach to Spatially Distributed Modeling of Carbon, Water, and
922 Nutrient Cycling. *Earth Interactions*, *8*(19), 1–42. https://doi.org/10.1175/1087-
923 3562(2004)8<1:RRHSSO>2.0.CO;2
924 Vargas, R., Sonnentag, O., Abramowitz, G., Carrara, A., Chen, J. M., Ciais, P., et al. (2013).
925 Drought Influences the Accuracy of Simulated Ecosystem Fluxes: A Model-Data Meta-
926 analysis for Mediterranean Oak Woodlands. *Ecosystems*, *16*(5), 749–764.
927 https://doi.org/10.1007/s10021-013-9648-1

928 Walter, M. T., Walter, M. F., Brooks, E. S., Steenhuis, T. S., Boll, J., & Weiler, K. (2000).
929 Hydrologically sensitive areas: Variable source area hydrology implications for water
930 quality risk assessment. *Journal of Soil and Water Conservation*, *55*(3), 277–284.
931 White, M. A., Thornton, P. E., Running, S. W., & Nemani, R. R. (2000). Parameterization and
932 Sensitivity Analysis of the BIOME–BGC Terrestrial Ecosystem Model: Net Primary
933 Production Controls. *Earth Interactions*, *4*(3), 1–85. https://doi.org/10.1175/1087-
934 3562(2000)004<0003:PASAOT>2.0.CO;2
935 Wohlgemuth, P. (2006). *Hillslope erosion and small watershed sediment yield following a*
936 *wildfire on the San Dimas Experimental Forest, southern California*. Reno, Nevada.:
937 Proceedings of the 8th Federal Interagency Sedimentation Conference. Retrieved from
938 https://www.semanticscholar.org/paper/HILLSLOPE-EROSION-AND-SMALL-
939 WATERSHED-SEDIMENT-A-ON-
940 Wohlgemuth/e666a9991c2c1813f3e63289a20636d4028fb7ec
941 Wood, E. F., Lettenmaier, D. P., & Zartarian, V. G. (1992). A land-surface hydrology
942 parameterization with subgrid variability for general circulation models. *Journal of*
943 *Geophysical Research: Atmospheres*, *97*(D3), 2717–2728.
944 https://doi.org/10.1029/91JD01786
945 Wood, E. F., Roundy, J. K., Troy, T. J., van Beek, L. P. H., Bierkens, M. F. P., Blyth, E., et al.
946 (2011). Hyperresolution global land surface modeling: Meeting a grand challenge for
947 monitoring Earth's terrestrial water. *Water Resources Research*, *47*(5).
948 https://doi.org/10.1029/2010WR010090

949 Zarnetske, J. P., Haggerty, R., Wondzell, S. M., & Baker, M. A. (2011). Dynamics of nitrate
950 production and removal as a function of residence time in the hyporheic zone. *Journal of*
951 *Geophysical Research: Biogeosciences*, *116*(G1). https://doi.org/10.1029/2010JG001356
952 Zhang, J., Cai, Z., & Müller, C. (2018). Terrestrial N cycling associated with climate and plant-
953 specific N preferences: a review. *European Journal of Soil Science*, *69*(3), 488–501.
954 https://doi.org/10.1111/ejss.12533
955 Zhu, Q., Schmidt, J. P., & Bryant, R. B. (2012). Hot moments and hot spots of nutrient losses
956 from a mixed land use watershed. *Journal of Hydrology*, *414–415*, 393–404.
957 https://doi.org/10.1016/j.jhydrol.2011.11.011
958 Zhu, Q., Schmidt, J. P., & Bryant, R. B. (2015). Maize (Zea mays L.) yield response to nitrogen
959 as influenced by spatio-temporal variations of soil–water-topography dynamics. *Soil and*
960 *Tillage Research*, *146*, 174–183. https://doi.org/10.1016/j.still.2014.10.006
961 Zhu, Q., Castellano, M. J., & Yang, G. (2018). Coupling soil water processes and the nitrogen
962 cycle across spatial scales: Potentials, bottlenecks and solutions. *Earth-Science Reviews*,
963 *187*, 248–258. https://doi.org/10.1016/j.earscirev.2018.10.005
964
965